IEEE Photonics Journal
An IEEE Photonics Society Publication

Open Access

A Surface Plasmon Resonance Temperature Sensing Unit Based on a Graphene Oxide Composite Photonic Crystal Fiber

Volume 12, Number 3, June 2020

Han Liang
Tao Shen
Yue Feng
Zhentao Xia
Hongchen Liu

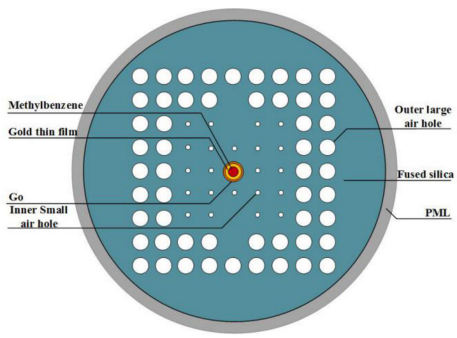

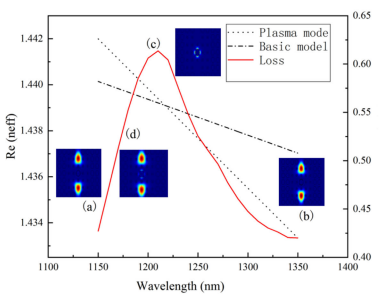

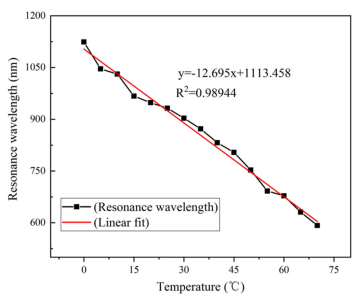

DOI: 10.1109/JPHOT.2020.2987809

A Surface Plasmon Resonance Temperature Sensing Unit Based on a Graphene Oxide Composite Photonic Crystal Fiber

Han Liang,[1,2] **Tao Shen**[1,2] **, Yue Feng,**[1,2] **Zhentao Xia,**[1,2] **and Hongchen Liu**[3]

[1]Heilongjiang Provincial Key Laboratory of Quantum Manipulation & Control, Harbin University of Science and Technology, Harbin 150080, China
[2]Key Laboratory of Engineering Dielectrics and Its Application, Ministry of Education, Harbin University of Science and Technology, Harbin 150080, China
[3]School of Electrical Engineering and Automation, Harbin Institute of Technology, Harbin 150001, China

DOI:10.1109/JPHOT.2020.2987809

Manuscript received March 6, 2020; revised April 3, 2020; accepted April 10, 2020. Date of publication April 15, 2020; date of current version May 26, 2020. This work was supported in part by the National Natural Science Foundation of China under Grant 51677044, in part by the Natural Science Foundation of Heilongjiang under Grant E2018047, and in part by the Outstanding Youth Innovation Foundation of Harbin under Grant 2017RAYXJ022. Corresponding author: Tao Shen (e-mail: taoshenchina@163.com).

Abstract: A twin-core sensor with high birefringence employing a photonic crystal fiber (PCF) is presented for simulated temperature measurements based on surface plasmon resonance (SPR). The internal wall of the central hole of the PCF is plated with gold and coated with graphene oxide (Au-GO) to develop an SPR sensing channel. The results of a numerical analysis with COMSOL Multiphysics show that the birefringence of this sensing structure can reach 0.0052. In addition, an average sensitivity of −12.695 nm/ °C can be achieved in the range of 0 °C∼80 °C. Compared with uncoated GO sensors and existing sensing units, this sensor shows improved stability, sensitivity and birefringence.

Index Terms: PCF, temperature sensing, GO, COMSOL.

1. Introduction

In recent decades, photonic crystal fibers (PCFs) have become a topic of interest in the field of optics [1], [2]. Because of desirable features such as their small size, lightweight, high sensitivity, corrosion resistance, design flexibility, good electrical insulation, and electromagnetic interference resistance [3], [4], PCFs have been extensively applied in biomedicine, environmental monitoring and control, chemical testing, food safety testing [5], [6] and other fields. After several generations of changes in sensing technology, PCF-based surface plasmon resonance (PCF-SPR) sensors have become a compelling focus of research [7]. The overall performance of PCFs [8] makes them suitable for broadband transmissions and various waveguide applications. They solve the problems of phase matching difficulty and physical parameter cross-sensitivity encountered in traditional optical fiber SPR sensors to a great degree. Hassani *et al.* [9] proposed one kind of PCR-SPR sensor, in which the inner wall of the air hole of the PCF was plated with a metal thin film and the test liquid filling the air hole was coupled to the surface plasmons excited by the metal film.

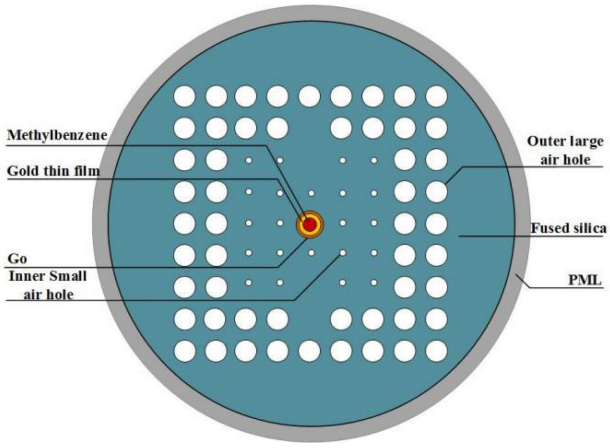

Fig. 1. Schematic diagram of the PCF structure.

Simulation results showed that the resolution of this sensor reached 10^{-4} Refractive Index Units (RIU).

Since Novoselov *et al*. [10], from the University of Manchester, UK, first produced monolithic graphene from graphite through micromechanical separation, research on graphene and its derivatives has become a topic of interest in recent years. About the techniques for preparing GO, many people made relevant reports. Preparation of GO would be posiible in a laboratory environment by applying Hummers'method [11], protein-assisted fabrication technique [12], chemical reduction [13]. An improved method [14] for preparing GO is introduced by Daniela C. Marcano *et al*. The new method does not generate toxic gases and the temperature is easy to control. It would be possible to deposit GO on PCF by applying simple chemical methods[15], one-step technique [16]. The use of metal materials on GO/graphene-coated PCFs could optimize the performance of traditional PCF-based sensors. For example, Kim *et al*. [17] used graphene as a substitute material for Au or Ag in SPR sensors and synthesized multilayer graphene films on Ni substrates to develop fiber optic sensors with increased sensitivity. In terms of optical fiber sensing, due to the advantages of the flexible design of the PCF structure and the high sensitivity of SPR sensing technology [18], [19], the sensitivity and precision of PCR-SPR sensors are higher than those of conventional fiber optic sensors. P. B. Bing *et al*. [20] prepared a PCF-SPR temperature sensor using a high-refractive-index glycerol liquid, achieving a low-temperature resolution as low as 4×10^{-6} RIU. Later, R. Boufenar *et al*. [21] filled elliptic stomata with liquid ethanol to design a PCF temperature sensor with high birefringence. However, despite the numerous studies on PCR-SPR temperature sensors, in engineering applications, the behavioral requirements for temperature sensors are more stringent.

Therefore, in this paper, we study a dual-hole core PCF-SPR temperature sensor with high birefringence. Combining SPR sensing technology with a PCF, a gold film is coated onto the inner wall of the PCF center hole, which is then further covered with GO and filled with toluene liquid with a high temperature sensitivity coefficient to realize sensing. The effects of the refractive index of the background substrate, the size of the air holes, and the thickness of the gold film are taken into consideration to ensure accuracy. The results can provide an experimental basis and theoretical reference for research and development concerning high-sensitivity PCF sensing units.

2. Model Structure

The full-vector finite element simulation software COMSOL Multiphysics was employed to design a PCF with a dual-hole core structure. A cross-sectional view of the designed PCF is shown in Fig. 1. This structure contains 5 layers of air holes, with a single small air hole of diameter d_c in the center of the structure. In order to introduce high birefringence in PCF, four layers of large

and small circular air holes are designed around the central air hole, which immensely destroys the central symmetry of PCF. In the second and third layers, two air holes are omitted, so that the mode field energy is concentrated at both ends to form a double-hole core. The air hole in the center of the structure is used as the sensing channel for SPR, and the inner sidewall is first plated with a gold metal layer and then covered with GO. After being injected with a highly temperature sensitive liquid, toluene, this sensing channel can be used for SPR by means of the Au-GO composite method to perform sensing analysis and research. The first two layers of air holes are smaller than the last two layers of air holes, which makes the evanescent wave contact the metal film more fully to improve the sensing sensitivity.

The interval between adjacent air holes, t_period, is fixed at 2.0 μm. The substrate of this PCF is fused silica; hence, the background substrate material is equivalent to quartz. The thickness of the gold metal thin film is t_Au. The thickness of the single-layer GO is very thin, only 0.34 nm. The outermost layer of the structure is a perfectly matched layer (PML), which is used to limit the propagation of light and control the light that is studied and analyzed in this PCF sensor.

For temperature sensing studies, the temperature of the substrate material must be considered. The analysis of this material is derived from the Sellmeier equation [22] shown in formula (1).

$$n^2(\lambda, T) = \left(1.31552 + 0.69754 \times 10^{-5} T\right) + \frac{\left(0.91316 + 0.548368 \times 10^{-6} T\right)}{\lambda^2 - 100} + \frac{\left(0.788404 + 0.235835 \times 10^{-4}\right)\lambda^2}{\lambda^2 - \left(0.0110199 + 0.584758 \times 10^{-6} T\right)} \tag{1}$$

where λ is the incident wavelength of the light in the optical waveguide, in microns, and T is the temperature, in Celsius. The relationship between the refractive index of the quartz substrate and the incident wavelength is nonlinear; accordingly, the refractive index of the quartz substrate calculated by formula (1) is reasonably consistent with the real situation.

Furthermore, the sensor is filled with toluene, a temperature-sensitive liquid material. Through external injection, we injected toluene into the small hole of the central sensing channel of the PCF-SPR sensor to form a sensing channel in combination with the composite Au-GO material layer. The refractive index of the toluene can also be obtained from a Sellmeier equation [23], as shown in formula (2).

$$n(\lambda) = 1.474775 + \frac{6990.31}{\lambda^2} + \frac{2.1776 \times 10^8}{\lambda^4} - \alpha_M (T - 20.15) \tag{2}$$

where λ is the incident wavelength of the light in the optical waveguide, in microns, and T is the temperature, in Celsius. α_{M} is the temperature sensitivity coefficient of toluene, and its value is 5.27310^{-4}/ °C. It is two orders of magnitude [24] higher than the temperature sensitivity coefficient of the substrate material, i.e., fused silica. As a result, the influence of external temperature changes on the refractive index of the fused silica can be ignored in this work.

Since the PCF proposed in this paper is center-symmetric and provides two polarization directions, X and Y, which are orthogonally distributed, the PCF-SPR sensor can simultaneously measure birefringence and temperature. The birefringence value B [25] is calculated by formula (3).

$$B = \left|\mathrm{Re}(n_{eff}^x) - \mathrm{Re}(n_{eff}^y)\right| \tag{3}$$

The confinement loss (α) is a key parameter index [26] that is proportional to the imaginary part of the effective mode refractive index and represents the ability of an optical waveguide to confine incident light. The equation is shown as formula (4).

$$\alpha = \frac{40 \times \pi \times imag(neff) \times 10^3}{\lambda \times \ln(10)} \mathrm{dB/cm} \tag{4}$$

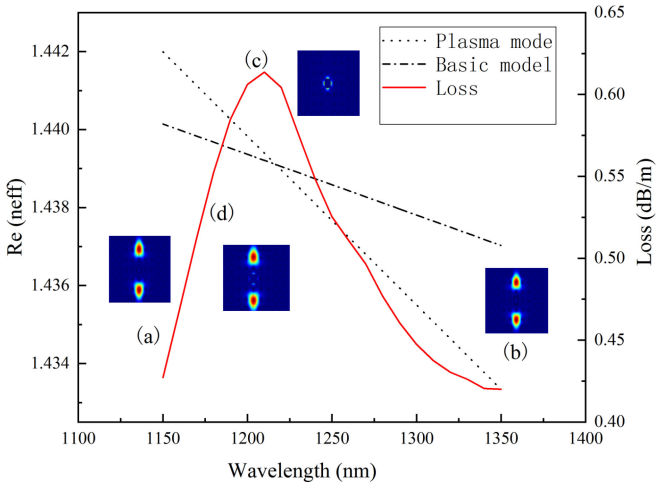

Fig. 2. Relationship between the effective mode refractive index, the fundamental mode loss spectrum, and the incident wavelength.

where λ represents the incident wavelength and imag(neff) represents the imaginary part of the effective refractive index. In addition to birefringence and confinement loss, the effective mode field area (A_{eff}) [27] is also a major parameter of a dual-core fiber; in fact, it is the starting point for understanding the nonlinear effects of PCFs. The definition is given in formula (5).

$$A_{eff} = \frac{\left|\iint |E(x,y)|^2 dxdy\right|^2}{\iint |E(x,y)|^4 dxdy} \tag{5}$$

where E(x, y) represents the transverse electric field component. A desired effective mode field area can be achieved through reasonable selection of the structural parameters of the PCF.

3. Results and Discussion

Fig. 2 depicts the behaviors of the refractive index and resonant spectrum for the SPR mode and the fundamental core-guided mode. The red curve represents the confinement loss of the dual-core fundamental mode. The black dotted line and the black dash-dotted line represent the real part of the effective mode refractive index for the SPR mode and the fundamental core-guided mode, respectively, which decreases as the incident wavelength increases for both modes. A distinct loss peak appears at 1220 nm due to the coupling between the core-guided mode and the SPR mode. The two black lines also intersect at 1200 nm, thus verifying the phase matching phenomenon. In addition, the four inset images corresponding to the four positions labeled (a), (b), (c), and (d) in Fig. 2 show the changes in the mode field in the PCF-SPR sensor with increasing wavelength. Inset (c) shows that the energy in the model of the PCF-SPR sensor has been fully transferred from the original dual-hole core structure to the boundary between the metal layer and the GO layer in the center hole when the plasma resonance effect is at its maximum.

The fiber geometry has a significant impact on the optical performance of the sensor. Fig. 3 depicts the loss spectra of the microstructured PCF sensor with different diameters d_1 of the small inner-layer air holes. The resonance wavelength gradually increases as the diameter d_1 increases from 0.6 μm to 1.35 μm in small increments of $\Delta\lambda_{d1} = 14$ nm. However, the peak value of the resonance loss simultaneously decreases considerably, with an amplitude variation of $\Delta dB_{d1} = 953$ dB/cm. The larger the diameter d_1 of the inner-layer air holes is, the greater the light confinement effect of the cladding is, resulting in less light leaking from the dual-hole core in the direction of the metal and GO layers. As a result, the resonance intensity is weakened.

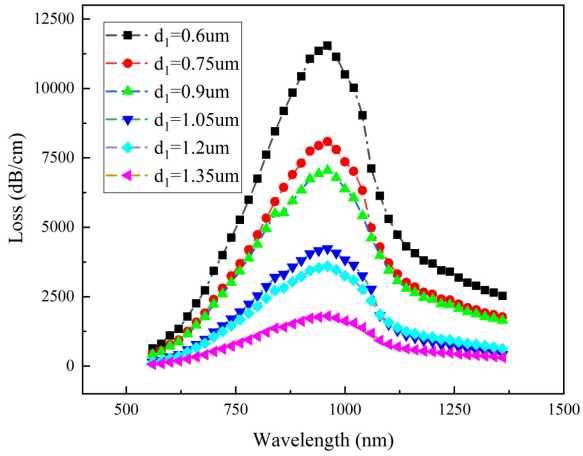

Fig. 3. Loss spectra of the PCF-SPR sensor with different diameters d_1 of the small inner-layer air holes, with the other parameters being $d_2 = 2\ \mu$m, $d_c = 2\ \mu$m, t_period $= 1.8\ \mu$m, t_Au $= 30$ nm, and t_G $= 1$.

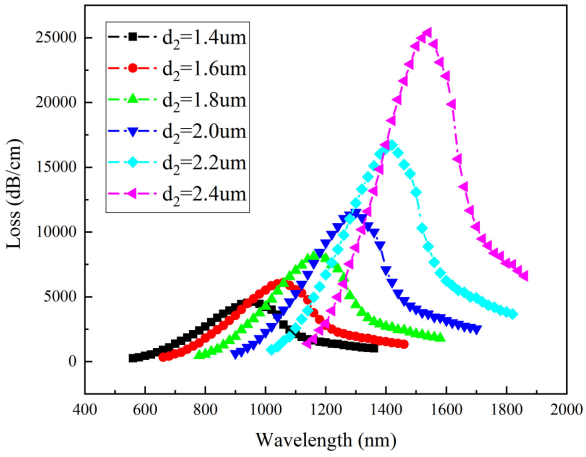

Fig. 4. Loss spectra of the PCF-SPR sensor corresponding to different diameters d_2 of the large outer-layer air holes, with the other parameters being $d_1 = 0.9\ \mu$m, $d_c = 2\ \mu$m, t_period $= 1.8\ \mu$m, t_Au $=$ 30 nm, and t_G $= 1$.

In Fig. 4, it is clear that as the diameter d_2 of the large outer-layer air holes increases from 1.4 μm to 2.4 μm, the resonance intensity increases and the resonance wavelength moves toward longer wavelengths, from 940 nm to 1540 nm, indicative of a redshift. The outer two layers of large air holes in the microstructured PCF-SPR optical waveguide constrain the optical wave loss and cause the evanescent wave to interact with the metal and GO layers with a high intensity. Accordingly, the constraining effect of the large outer-layer air holes on the evanescent wave is significantly stronger than that of the small inner-layer air holes, resulting in a continuous increase in the loss value with increasing d_2 when the diameter d_1 of the small air holes in the inner two layers is fixed. Unlike in Fig. 3, there is also an obvious shift in the resonance wavelength. Similarly, the changes in the loss spectrum that are caused by altering the diameter d_c of the air hole for the center sensing channel are shown in Fig. 5.

The loss spectrum shows a positive shift in the resonance peak with an increase in the diameter d_c. For instance, the pink curve, corresponding to the maximum d_c, is shifted toward longer wavelengths, whereas the black curve, corresponding to the smallest d_c, is shifted toward shorter wavelengths. As d_c increases, a stronger constraint is placed on the light field energy of the fundamental mode in the waveguide. Accordingly, under the action of the evanescent field, the

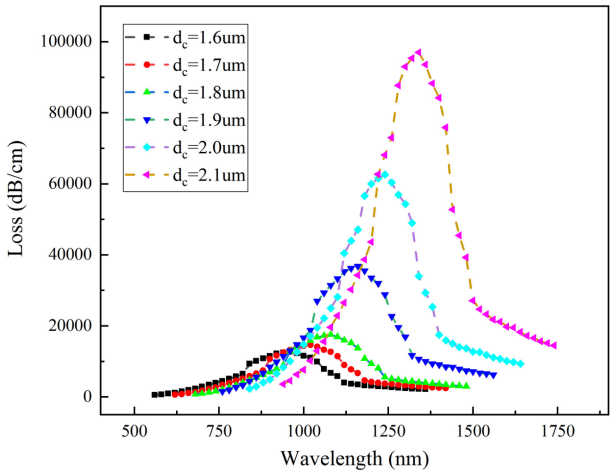

Fig. 5. Loss spectra of the PCF-SPR sensor corresponding to different diameters d_c of the central sensing channel, with the other parameters being $d_1 = 0.9\ \mu$m, $d_2 = 2.2\ \mu$m, t_period $= 1.8\ \mu$m, t_Au $= 30$ nm, and t_G $= 1$.

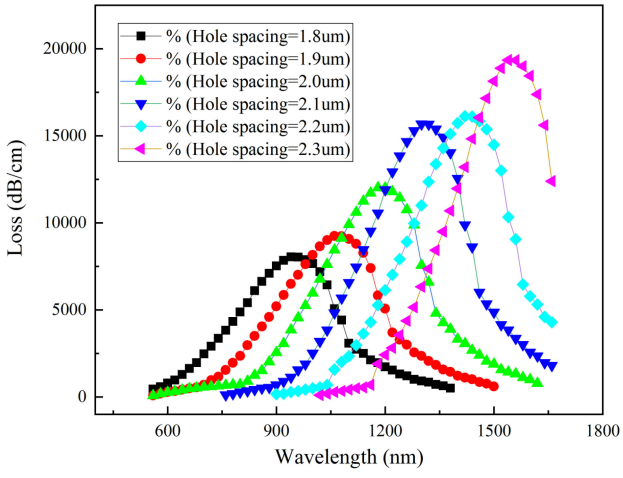

Fig. 6. Loss spectra of the PCF-SPR sensor corresponding to different air hole spacings t_period, with the other.

energy transferred from the fundamental mode to the surface of the metal layer increases when the effective refractive index of the fundamental mode is the same as that of the metal- and GO-coated surface, that is, when phase matching occurs. Therefore, it is reasonable to infer that the resonance peak in the sensor's loss spectrum will become steeper as the center hole diameter d_c increases.

Fig. 6 depicts the loss peaks of the basic mode for different values of the air hole spacing, t_period. The resonance peak increases in amplitude from 7724 dB/cm to 19672 dB/cm, becoming higher and narrower, as the air hole spacing increases from 1.8 μm to 2.3 μm. Furthermore, the resonance wavelength redshifts from 935 nm to 1526 nm as the air hole spacing changes from 1.8 μm to 2.3 μm. The spatial period of the air holes determines the distribution of the evanescent field in the optical waveguide and thus affects the plasmon resonance of the evanescent wave with the gold- and GO-coated surface. Therefore, the behavior of the designed sensor can be optimized by adjusting the air hole spacing.

In addition to the structural parameters of the PCF, the impact of the thickness of the gold layer on the loss spectrum was studied, and the corresponding results are shown in Fig. 7. As the thickness

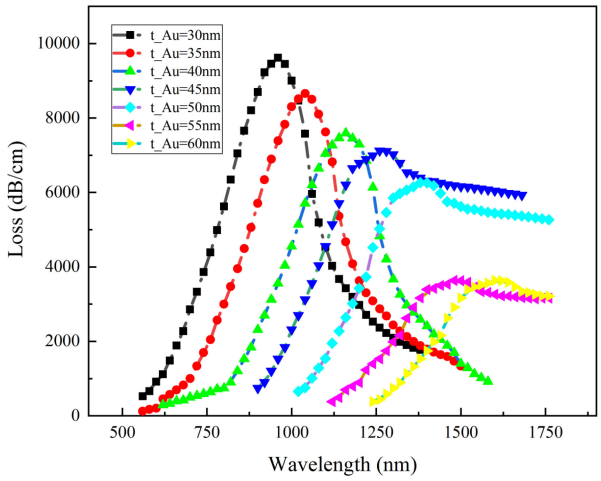

Fig. 7. Loss spectra of the PCF-SPR sensor corresponding to different thicknesses t_Au of the metal layer, with the other parameters being $d_1 = 0.9\ \mu$m, $d_2 = 2.2\ \mu$m, $d_c = 2.1\ \mu$m, t_period $= 2.1\ \mu$m, and t_G $= 1$.

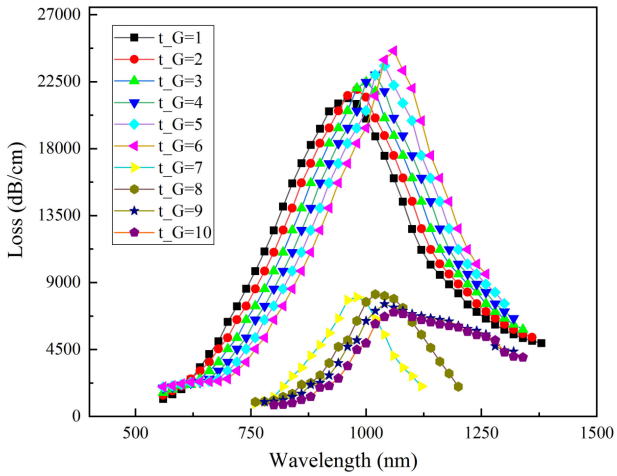

Fig. 8. Loss spectra of the PCF-SPR sensor corresponding to different graphene thicknesses t_G, with the other parameters being $d_1 = 0.9\ \mu$m, $d_2 = 2.2\ \mu$m, $d_c = 2.1\ \mu$m, t_period $= 2.1\ \mu$m, and t_Au $=$ 35 nm.

of the gold metal layer increases from 30 nm to 60 nm, the height of the loss peak decreases from 9675 dB/cm at 30 nm to 3507 dB/cm at 60 nm. As the gold film becomes thicker, the evanescent wave excited by the evanescent field has more difficulty crossing the surface of the metal to excite SPR with the metal in the sensing channel, resulting in a weakened SPR response. Therefore, the thickness of the gold film also has a vital influence on the surface plasmonic waves.

Fig. 8 presents the wavelength dependence of the loss spectrum on the number of GO layers, t_G. The resonance wavelength can be tuned between 940 nm and 1060 nm with t_G $=$ 1–7, whereas it varies from 975 nm to 1050 nm in the range of t_G $=$ 8–10. This is because GO is more sensitive in the mid-infrared band; hence, the possible positions of the resonance loss peak of this microstructured PCF-SPR sensor system are also mostly concentrated in this band. As t_G increases, the amplitude of the resonance peak increases from 21046 dB/cm at t_G $= 1$ to 24937 dB/cm at t_G $= 7$. In contrast, as t_G further increases, the peak amplitude steeply decreases from 7513 dB/cm at t_G $= 8$ to 6247 dB/cm at t_G $= 10$. The physical interpretation that underlies that phenomenon is that once the number of GO layers exceeds 6, the absorption characteristics of

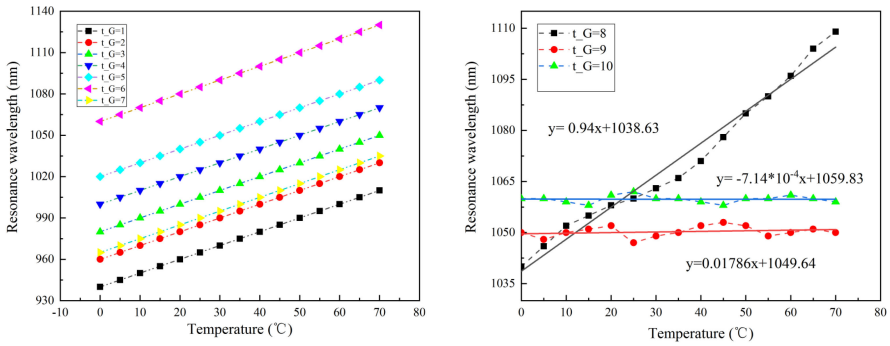

(a) t_G=1-7 (b) t_G=8-10

Fig. 9. Temperature sensing diagrams showing the variation in the resonance wavelength with temperature for different GO thicknesses, with the other parameters being $d_1 = 0.9$ μm, $d_2 = 2.2$ μm, $d_c = 2.1$ μm, t_period $= 2.1$ μm, and t_Au $= 35$ nm.

GO begin to decrease, and simultaneously, its properties become closer to those of carbon atoms. When the number of GO layers reaches approximately 10, the peak value of the loss will be low, and the resonance will gradually weaken.

Fig. 9 further illustrates the dependence of the resonance wavelength on the number of GO layers. When the number of GO layers is sufficiently small, a redshift occurs in the resonance wavelength with an increase in t_G, and a gradual redshift with increasing temperature is also observed, as shown in Fig. 9(a). It should also be noted that the nature of the GO itself changes in a stepwise manner and slowly approaches that of carbon atoms as the number of GO layers increases; as a result, an abrupt change in the trend is observed for the temperature sensing curve at t_G $= 7$, which is close to the curve at t_G $= 2$. Fig. 9(b) shows the temperature sensing diagram for higher GO thicknesses, which is notably different from that for fewer GO layers. The results of linear fitting and numerical calculation indicate that the sensing curve for t_G $= 7$ is similar to that for t_G $= 8$. Moreover, the sensing curves for t_G $= 9$ and t_G $= 10$ tend to be flat, showing only tiny the variations in the resonance wavelength. The phenomenon of the joint excitation of SPR by the GO and gold film still exists, but it is relatively not obvious, as the properties of the GO are close to those of carbon atoms.

Because this article studies the performance of SPR temperature sensing with Au as the excitation source for SPR, the characteristics of the Au material directly determine the performance of the sensor. Hence, it is imperative to examine the effect of the thickness of the gold thin film, t_Au, on the effective mode field area. The corresponding results are depicted in Fig. 10. The effective mode field area in the PCF waveguide lens increases as the temperature and thickness of the gold thin film increase. It is worth pointing out that the cumulative curve of the effective mode field area shows an abrupt rise once the temperature increases above 45 °C. The explanation for this behavior is that the refractive index of toluene, a temperature-sensitive liquid, decreases with increasing temperature and approaches the refractive index of the fused silica, thus reducing the difference in refractive index between the cladding and the dual-hole core and resulting in a decrease in the constraining effect on the light. We also inspected the dependence of the chromatic dispersion on the temperature, which is plotted as the red dotted line in Fig. 10. An increase in temperature results in a decrease in chromatic dispersion.

In summary, considering the actual benefits of the microstructured optical waveguide and the challenges arising in actual fabrication and grinding, the following parameters are recommended: $d_1 = 0.9$ μm, $d_2 = 2.2$ μm, $d_c = 2.1$ μm, t_period $= 2.1$ μm, t_Au $= 35$ nm, t_G $= 3$, and temperature $\leq$65 °C.

Fig. 11 shows the temperature sensitivity curves of microstructured PCF-SPR sensing units. Fig. 11(a) shows the fitted temperature curve of the proposed PCF sensing unit with GO, for which a linear correlation coefficient of 0.098944 is calculated. The curve for a corresponding sensor

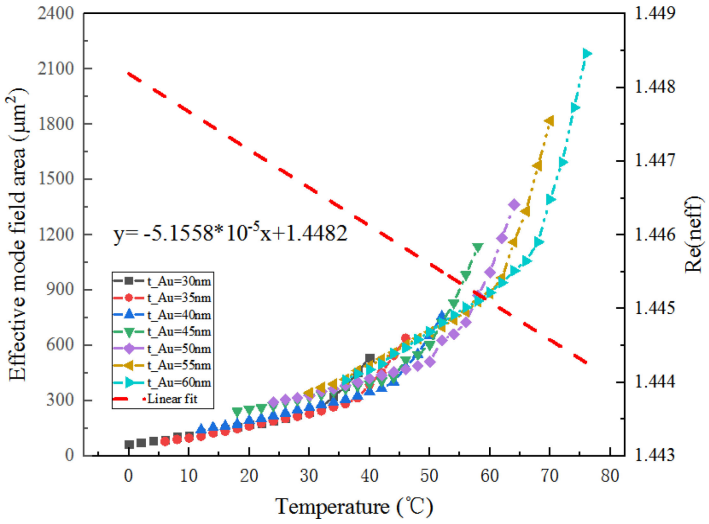

Fig. 10. Temperature sensing diagrams showing the variation in the effective mode field area with temperature for different metal layer thicknesses t_Au, with the other parameters being $d_1 = 0.9$ μm, $d_2 = 2.2$ μm, $d_c = 2.1$ μm, t_period $= 2.1$ μm, t_Au $= 35$ nm, and t_G $= 3$.

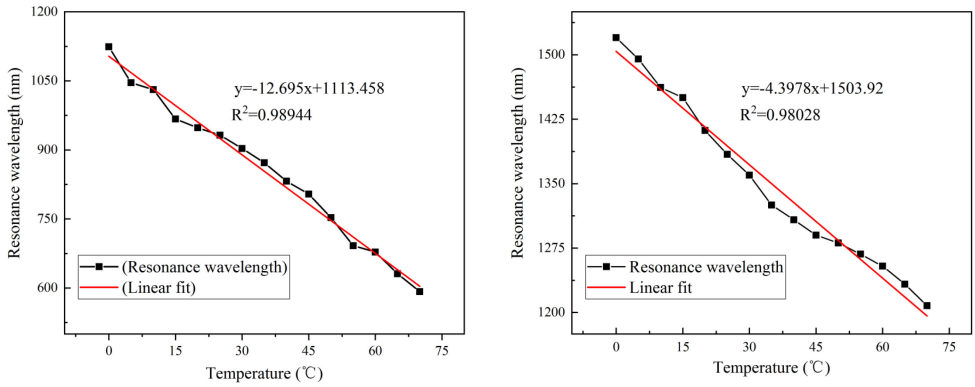

(a) PCF-SPR+GO (b) PCF-SPR

Fig. 11. Temperature sensitivity curves of the microstructured PCF-SPR sensing system.

without GO coating is shown in Fig. 12(b). It is observed that the linear correlation coefficient for this sensor is slightly lower than that for the GO-coated sensing unit. For comparison, the average sensitivity in the temperature range from 0 °C to 70 °C of the composite Au-GO sensing system is -12.695 nm/ °C, whereas that of the sensor without GO is -4.3978 nm/ °C. Under the assumption that changes in the range of $\Delta\lambda_{\min} = 0.1$ nm can be captured through spectral analysis, the resolution [28] of the temperature sensor can be defined by formula (6):

$$R = \Delta T \frac{\Delta\lambda_{\min}}{\Delta\lambda_{peak}} \tag{6}$$

where $\Delta\lambda_{\text{peak}}$ represents the change in the resonance wavelength. Numerical calculations indicate that the resolution of the proposed PCF-SPR sensor is 0.00725 °C. Compared with the previously reported PCF temperature sensors, the PCF-SPR temperature sensor proposed in this paper shows significantly higher temperature sensitivity, as seen in Table 1.

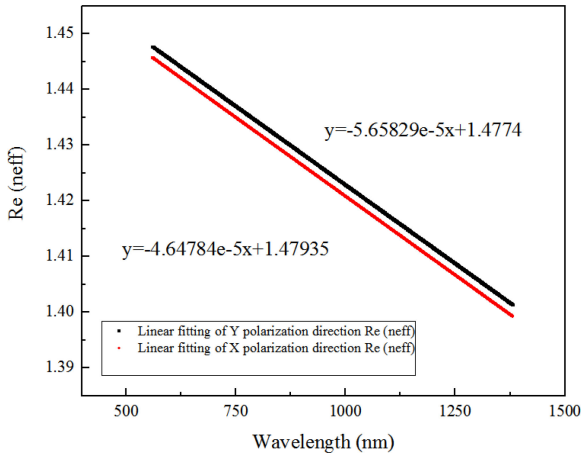

Fig. 12. Variations in birefringence and wavelength in the X and Y directions with parameters of $d_1 = 0.9\ \mu$m, $d_2 = 2.2\ \mu$m, $d_c = 2.1\ \mu$m, t_period $= 2.1\ \mu$m, t_Au $= 35$ nm, and t_G $= 3$.

TABLE 1
The Temperature Sensing Performance of Silver Nanowires PCF in [29], Liquid-Filled PCF in [28], Alcohol-Filled PCF in [30], Hexagonal PCF in [31], and the Proposed PCF

	Sensitivity (nm/℃)	Resolution (℃)	Birefringence	Ref
Silver nanowires PCF	2.7	-	-	[29]
Liquid-filled PCF	3.08	0.01325	-	[28]
Alcohol-filled PCF	6.6	-	$0.35*10^{-3}$	[30]
Hexagonal PCF	-11	-	$0.0868*10^{-3}$	[31]
Our proposed PCF with GO	-12.695	0.00725	$5.2*10^{-3}$	
Our proposed PCF without GO	-4.3978	-	-	

4. Conclusions

This paper proposes a new microstructured PCF-SPR temperature sensor with a dual-hole core. The asymmetric structure design and the deposition of a GO layer on the metal-coated surface to form a Au-GO composite structure not only protect the metal surface from easily becoming oxidized but also greatly improve the sensitivity and birefringence of the sensor. The full-vector finite element software COMSOL Multiphysics was applied to analyze the relationship between the resonance wavelength in the loss spectrum and the temperature given different air hole sizes, air hole spacings, metal layer thicknesses and GO thicknesses in the PCF sensor. Numerical analysis results show that the birefringence of the sensing structure can reach 0.0052. Additionally, the sensor can achieve an average sensitivity of -12.695 nm/ °C in the temperature range of 0 °C to 80 °C, and the corresponding resolution is 0.00725 °C, which is higher than that of a similar sensor unit without GO. The PCF-SPR temperature sensor proposed in this paper offers greatly improved temperature sensing performance, and the results reported here could serve as a theoretical basis and guidance for future experimental research.

References

[1] B. K. Paul, S. Chakma, M. Khalek, and K. Ahme, "Silicon nano crystal filled ellipse core based quasi photonic crystal fiber with birefringence and very high nonlinearity," *Chin. J. Phys.*, vol. 56, pp. 2782–2788, 2018.

[2] J. F. Liao, Y. M. Xie, X. H. Wang, D. B. Li, and T. Y. Huang, "Ultra-flattened nearly-zero dispersion and ultrahigh nonlinear slot silicon photonic crystal fibers with ultrahigh birefringence," *Photon. Nanostruct. Fundam. Appl.*, vol. 25, pp. 19–24, 2017.

[3] M. Liu, J. Y. Hou, X. Yang, B. Y. Zhao, and P. Shum, "Design of photonic crystal fiber with elliptical air-holes to achieve simultaneous high birefriengence and nonlinearity," *Chin. Phys. B.*, vol. 27, 2018, Art. no. 014206.

[4] Q. Liu, L. Xin, and Z. Wu, "Refractive index sensor of a photonic crystal fiber Sagnac interferometer based on variable polarization states," *Appl. Phys. Express*, vol. 12, 2019, Art. no. 062009.

[5] C. Liu *et al.*, "Numerical analysis of a photonic crystal fiber based on a surface plasmon resonance sensor with an annular analyte channel," *Opt. Commun.*, vol. 382, pp. 162–166, 2017.

[6] A. A Rifat, K. Ahmed, S. Asaduzzaman, B. K. Paul, and R. Ahmed, *Development of Photonic Crystal Fiber-Based Gas/Chemical Sensors*, Berlin, Germany: Springer, 2019, pp. 287–317.

[7] M. N. Sakib *et al.*, "High performance dual core D-shape PCF-SPR sensor modeling employing Gold coat," *Results. Phys.*, vol. 15, 2019, Art. no. 102788.

[8] K. Ahmed, B. K. Paul, M. A. Jabin, and B. Biswas, "FEM analysis of birefringence, dispersion and nonlinearity of graphene coated photonic crystal fiber," *Ceram. Int.*, vol. 45, pp. 15343–15347, 2019.

[9] A. Hassani and M. Skorobogatiy, "Design criteria for microstructured-optical-fiber-based surface-plasmon-resonance sensors," *J. Opt. Soc. Am. B: Opt. Phys.*, vol. 24, pp. 1423–1429, 2007.

[10] A. K. Geim and K. S. Novoselov, *The Rise of Graphene/Nanoscience and Technology: A Collection of Reviews from Nature Journals*. Singapore: World Scientific. 2010, pp. 11–19.

[11] W. S. Hummers and R. E. Offeman, "Preparation of graphitic oxide," *J. Am. Chem. Soc.*, vol. 80, no. 1958, Art. no. 1339.

[12] Z. H. Sheng, L. Song, J. X. Zheng, and D. H. Hu, "Protein-assisted fabrication of nano-reduced graphene oxide for combined in vivo photoacoustic imaging and photothermal therapy," *Biomaterials*, vol. 34, pp. 5236–5243, 2013.

[13] S. Stankovich, D. A. Dikin, R. D. Piner, and K. A. Kohlhaas, "Synthesis of graphene-based nanosheets via chemical reduction of exfoliated graphite oxide," *Carbon*, vol. 45, pp. 1558–1565, 2007.

[14] D. C. Marcano *et al.*, "Improved synthesis of graphene oxide," *ACS Nano.*, vol. 4, pp. 4806–4814, 2010.

[15] J. N. Dash, N. Negi, and R. Jha, "Graphene oxide coated PCF interferometer for enhanced strain sensitivity," *J. Lightw. Technol.*, vol. 35, pp. 5385–5390, 2017.

[16] R. M. Gerosa, P. G. Vianna, S. H. Domingues, and C. J. S. de Matos, "Reduced graphene oxide coated photonic crystal fiber for all-fiber laser mode locking," in *Proc. Conf. Lasers Electro-Opt.*, 2019, pp. 1–2, doi: 10.23919/CLEO.2019.8749586.

[17] J. Kim, G. Liu, Y. Lu, and L. Lee, "Intra-particle plasmonic coupling of tip and cavity resonance modes in metallic apertured nanocavities," *Opt. Express*, vol. 13, pp. 8332–8338, 2005.

[18] N. Chen, M. Chang, X. D. Zhang, J. Zhou, X. L. Lu, and S. L. Zhuang, "Highly sensitive plasmonic sensor based on a dual-side polished photonic crystal fiber for component content sensing applications," *Nanomaterials*, vol. 9, 2019, Art. no. 1587.

[19] X. Y. Wang, S.G. Li, Q. Liu, G. Y. Wang, and Y. Y. Zhao, "Design of a single-polarization single-mode photonic crystal fiber filter based on surface plasmon resonance," *Plasmonics*, vol. 12, pp. 1325–1330, 2017.

[20] P. B. Bing, Z. Y. Li, J. Q. Yao, Y. Lu, and Z. G. Di, "A photonic crystal fiber based on surface plasmon resonance temperature sensor with liquid core," *Mod. Phys. Lett. B.*, vol. 26, 2012, Art. no. 1250082.

[21] R. Boufenar, M. Bouamar, and A. Hocini, "Numerical analysis of highly birefringent photonic crystal fiber for temperature sensing application," *Photon. Nanostruct. Fundam. Appl.*, vol. 24, pp. 47–52, 2017.

[22] Q. Liu, S. G. Li, H. L. Chen, J. S. Li, and Z. K. Fan, "High-sensitivity plasmonic temperature sensor based on photonic crystal fiber coated with nanoscale gold film," *Appl. Phys. Express*, vol. 8, 2015, Art. no. 046701.

[23] Q. Wu, Z. Y. Zhang, X. C. Guo, and W. H. Shi, "Simultaneous measurement of magnetic field and temperature based on photonic crystal fiber with eliminating cross-sensitivity," *Acta. Physica Sinica.*, vol. 67, 2018, Art. no. 184212.

[24] Y. Q. Yu *et al.*, "Some features of the photonic crystal fiber temperature sensor with liquid ethanol filling," *Opt. Express*, vol. 18, pp. 15383–15388, 2010.

[25] M. Liu, H. T. Yuan, P. Shum, C. Shao, H. N. Han, and L. H. Chu, "Simultaneous achievement of highly birefringent and nonlinear photonic crystal fibers with an elliptical tellurite core," *Appl. Opt.*, vol. 57, pp. 6383–6387, 2018.

[26] A. A. Rifat, G. A. Mahdiraji, D. M. Chow, Y. G. Shee, R. Ahmod, and F. R. Adikan, "Photonic crystal fiber-based surface plasmon resonance sensor with selective analyte channels and graphene-silver deposited core," *Sensors*, vol. 15, pp. 11499–11510, 2015.

[27] T. Y. Yang, E. Wang, H. M. Jiang, Z. J. Hu, and K. Xie, "High birefringence photonic crystal fiber with high nonlinearity and low confinement loss," *Opt. Express*, vol. 23, pp. 8329–8337, 2015.

[28] C. Liu *et al.*, "A highly temperature-sensitive photonic crystal fiber based on surface plasmon resonance," *Opt. Commun.*, vol. 359, pp. 378–382, 2016.

[29] Y. Lu, M. T. Wang, C. J. Hao, Z. Q. Zhao, and J. Q. Yao, "Temperature sensing using photonic crystal fiber filled with silver nanowires and liquid," *IEEE Photon. J.*, vol. 6, no. 3, Jun. 2014, Art. no. 6801307.

[30] W. W. Qian *et al.*, "High sensitivity temperature sensor based on an alcohol-filled photonic crystal fiber loop mirror," *Opt Lett.*, vol. 36, pp. 1548–1550, 2011.

[31] Y. E. Monfared, C. Liang, R. Khosravi, B. Kacerovska, and S. Yang, "Selectively toluene-fifilled photonic crystal fifiber Sagnac interferometer with high sensitivity for temperature sensing applications," *Results Phys.*, vol. 13, 2019, Art. no. 102297.